Development of a photoelectron spectrometer for hard x-ray photon diagnostics

Joakim Laksman, Florian Dietrich, Jia Liu, et al.

View Online   Export Citation   CrossMark

Development of a photoelectron spectrometer for hard x-ray photon diagnostics

View Online   Export Citation   CrossMark

Joakim Laksman,[1,a] (iD) Florian Dietrich,[1] Jia Liu,[1] (iD) Theophilos Maltezopoulos,[1] Marc Planas,[1]
Wolfgang Freund,[1] Randeer Gautam,[1] Naresh Kujala,[1] (iD) Sonia Francoual,[2] (iD) and Jan Grünert[1] (iD)

AFFILIATIONS

[1] European XFEL, Holzkoppel 4, 22869 Schenefeld, Germany
[2] Deutsches Elektronen-Synchrotron DESY, Notkestraße 85, 22607 Hamburg, Germany

[a] Author to whom correspondence should be addressed: joakim.laksman@xfel.eu

ABSTRACT

The development and characterization of an angle-resolved photoelectron spectrometer, based on the electron time-of-flight concept, for hard x-ray photon diagnostics at the European Free-Electron Laser, are described. The instrument is meant to provide users and operators with pulse-resolved, non-invasive spectral distribution diagnostics, which in the hard x-ray regime is a challenge due to the poor cross-section and high kinetic energy of photoelectrons for the available target gases. We report on the performances of this instrument as obtained using hard x-rays at the PETRA III synchrotron at DESY in multibunch mode. Results are compared with electron trajectory simulations. We demonstrate a resolving power of 10 eV at incident photon energies up to at least 20 keV.

Published under an exclusive license by AIP Publishing. https://doi.org/10.1063/5.0097525

I. INTRODUCTION

The unique properties of x-ray Free-Electron Laser (XFEL) radiation offering high-intensity and coherent x-ray pulses at Ångström wavelengths and pulse duration of a few femtoseconds have found applications where the ability to take snapshots of samples at unprecedented molecular length and time scales provides new scientific insights. However, the stochastic nature of Self-Amplification of Spontaneous Emission (SASE) has the consequence that every photon pulse displays individual characteristics in terms of spectral distribution and intensity. Modern XFEL facilities require photon diagnostics instrumentation capable of handling SASE fluctuations and of providing relevant single-shot beam parameters to users and operators.[1–3]

At the European XFEL (EuXFEL) facility in Schenefeld, Germany, the x-ray photon diagnostics group (XPD) utilizes a variety of dedicated techniques for providing beam parameters.[4] Two non-invasive techniques based on the principle of photoionization of dilute gas targets are

(1) The X-ray Gas Monitor (XGM) for pulse energy and beam position diagnostics.[5,6]
(2) In the case of soft x-rays, the angle-resolved Photo-Electron Spectrometer (PES) designed at the PETRA III, P04 beamline

at DESY,[7] with 16 electron Time-Of-Flight (eTOF) flight-tubes as dispersive elements provide pulse resolved photon energy and polarization diagnostics.[8]

Electron spectrometers based on the eTOF principle have flight-tubes with applied voltages that decelerate the electrons. Fast electronics register the time difference from ionization to detection, which is related to the kinetic energy of the photoelectrons. The PES, which uses dilute gas targets, is completely non-invasive in contrast to complementary grating-based spectral diagnostics techniques[9] and has found applications for soft x-ray photon diagnostics and experiments.[10–17] Adapting the PES concept to the hard x-ray range is not straightforward and is challenged in that regime by the following: (1) Poor ionization cross-section leads to lower statistics for single shots. (2) Very high kinetic energies of photoelectrons, corresponding to a significant fraction of the speed of light, with tough demands on the flight-tube potentials. One solution to increase the resolving power of the eTOF, also for very high kinetic energies, is to employ long flight-tubes, up to ~1 m,[18,19] but due to the limited space in the EuXFEL tunnel, which constraints our flight-tube lengths from the source point to the detector to a maximum of 250 mm this is not an option and we had to find a different approach. Moreover, the restricted access to the tunnel and the need for

continuous operation calls for a robust and low-maintenance design. To be able to fulfill the user requirement of non-invasive, single-shot spectral distribution with a resolution of ~10 eV at photon energies up to at least 20 keV, a novel flight-tube concept had to be developed with specific electron optics for simultaneously strong retardation and precise focusing. This paper describes the development of the new PES dedicated to photon diagnostics at hard x-rays and presents results from test measurements at the resonant diffraction beamline P09 at PETRA III with x-rays at photon energies in the range from 10 to 20 keV.[20]

II. INSTRUMENT

A. Design

A CAD model cross-section view of our design is presented in Fig. 1. The spectrometer consists of 12 eTOF flight-tubes oriented perpendicular to the x-ray beam at angles of $[0°, 30°, \ldots, 330°]$. In order to maximize, the flight-tubes performance as dispersive elements, while simultaneously focusing the photo-emitted electrons to the detector, we opted for a design where the flight-tubes are divided in *retardation region* and *Einzel lens*, separated with a high transmission (90%) gold mesh to prevent field penetration between the two regions:

(1) An effusive gas jet is injected via a capillary in the Interaction Region (IR) where it interacts with the x-ray beam and photoelectrons are emitted. The IR has a ø35 mm inner cylindrical diameter and encapsulates the source region to make it field-free. Following the IR is nine 2 mm thick electrodes labeled [Ret 1, Ret 2, . . . Ret 9] where gradually higher potentials are applied. These ten first electrodes are serial connected via 100 MΩ resistors to work as voltage dividers, thus within a short distance, a steep retardation is imposed,

capable of decelerating electrons from many keV to only a few 10 eV.

(2) Following the strong deceleration, electrons must be guided to the detector, which is achieved by a three-element electrostatic Einzel lens with electrodes labeled [Einz 1, Einz 2, and Einz 3]. In front of the detector, an additional gold mesh is placed on the same potential as the final element in the flight-tube.

Due to hardware limitations, the maximum voltage that can be applied on an electrode is an absolute value of 10 kV. In order to exceed this value and detect even higher electron kinetic energies, we have the option to apply a positive voltage on the source region and a negative voltage on the end of the retardation region, thus enabling significantly higher retardation without dielectric breakdown. In this configuration, we have to apply the same potential, as in the source region, on the capillary that is electrically isolated via a ceramic pipe from the XYZ stage manipulator where it is mounted. For a robust monolithic design, flight-tubes were machined out of aluminum so that each electrode segment is a block with 12 conical holes that work as parts of the flight-tube. Electrodes are separated by 1 mm from each other with PEEK spacers. To avoid oxidation, aluminum parts were chromatized with the surface treatment *SurTec* 650, which ensures the preservation of the electrical conductivity. On each side of the flight-tube assembly, we have aluminum disks that work as shields. The vacuum vessel is made of non-magnetic stainless steel, and care has been taken that all parts are non-magnetic. A 3D Helmholtz coil structure encloses the device and is used to compensate for the background magnetic field which otherwise would influence the electron trajectories. A fluxgate-type magnetometer (*Bartington Mag-03*) to monitor the magnetic field is mounted in a pocket flange to be as close as possible to the source region. The detectors are *Hamamatsu F9892-31* Micro Channel Plates (MCP) with 42 mm
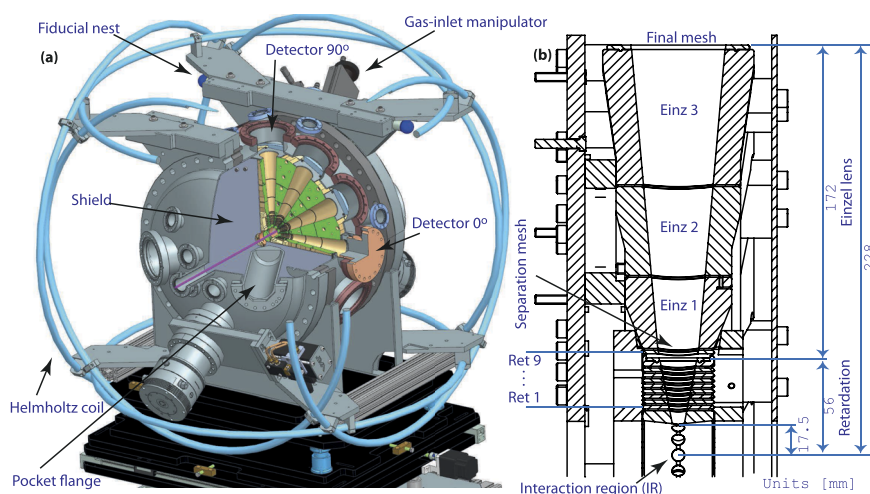
FIG. 1. (a) Cross-section computer rendering of the hard x-ray PES. The purple beam illustrates x-ray pulses through the interaction region. A target gas is injected into the center. Emitted photoelectrons are decelerated and focused through the electron optics of the 12 flight-tubes before they reach the detector. Helmholtz coils encapsulate the device to cancel external magnetic fields that are monitored by a magnetometer placed in the pocket flange, which otherwise influences the electron trajectories. Aluminum discs are mounted on both sides as shields to block electromagnetic fields. (b) Inside view of one flight-tube. The photo-reaction takes place in the interaction region. Photo-emitted electrons are decelerated in the retardation region and focused to the detector in the Einzel lens region.

active area and 0.7 ns pulse width. For alignment of the instrument to the beam, the setup is supported by decoupled transverse and vertical translation motion controlled by stepper motors. Six fiducials are placed on the chamber to enable pre-alignment by a laser tracker.

A target gas that is typically a noble gas is injected as an effusive jet in the interaction region via a ø100 μm inner-diameter capillary. Target gas criteria are high cross section (σ),[21–26] low natural line-width (Γ),[27] and binding energy (E_B)[28] that gives a low kinetic energy (E_K) for a particular photon energy ($h\nu$) according to the photoelectric effect, $E_K = h\nu - E_B$. In the case of polarization studies, also an anisotropy parameter (β) far from 0 becomes relevant.[29,30] Furthermore, the presence of Auger lines can be valuable for kinetic energy calibration of the spectrum.

During the last decade, Hard x-ray Photoelectron Spectroscopy (HAXPES) on low-density matter samples has emerged as a spectroscopic technique well suited to probe the electronic properties and provide the precise binding energies of gases.[31,32] In the region 4800–14 400 eV, xenon is the most suitable target gas for the PES with three photo lines: 2s, 2p$_{1/2}$, and 2p$_{3/2}$. Measured natural line-widths have most recently been reported by Oura *et. al.*[33] Xe 1s photoionization and subsequent Auger decay have been studied by Piancastelli *et al.*[34] Above 14 400 eV, krypton 1s is the best choice. Theoretical and experimental photoionization cross section has been published by Schaphorst *et al.*[35] Photoionization binding energy and natural line-width have recently been reported by Boudjemia *et al.*[36] E_B and Γ for xenon and krypton are presented in Table I.

Before installation in the EuXFEL SASE1 tunnel, the device was tested at the tender and hard x-ray beamline P09 at PETRA III, DESY, which offers high energy tuneability from 2.7 to 24 keV, full polarization control, high energy resolution, and flux.[20] The device was placed in the open port third experimental hutch (EH3). The Si(111) crystal monochromator with the energy bandwidth 1.3×10^{-4} was selected. The beam was uncollimated of size ~2.1 × 1.5 mm² (V × H) FWHM, and mirrors were used to suppress higher harmonics. Measurements were carried out when the machine was operating in timing mode at 5.2 MHz (192 ns pulse separation). For data acquisition, a programmable four channel *Lecroy WavePro 725Zi* 2.5 GHz and 40 GS/s oscilloscope was used. Prior to the oscilloscope pre-amplifiers were used (*Minicircuits ZFL-1000LN+*) that enhance the MCP detector signal and also protect the oscilloscope channels from possible overvoltages. For additional signal matching, the signal chain contains 3 dB attenuators at the

input of the pre-amplifiers and 10 dB attenuators at the input of the oscilloscope.

B. Simulations

The CAD model was imported into the commercial software *SIMION 8.0* for electron trajectory simulations in order to quantify the performance and improve the design prior to manufacturing. The method is *Runge-Kutta* with relativistic velocity corrections. Electrodes were simulated with 0.1 mm³ resolution. Much effort was invested in replicating actual experimental conditions as realistically as possible in terms of typical target gases and photon energies, by optimizing the voltage settings for the instrumental broadening, the resolving power, and the collection efficiency of the device. Figures 2(a) and 2(b) show cross-section views of the model in SIMION with a few simulated electron traces at two different initial kinetic energies. Retardation voltage (V_R) that is defined as the difference in potential between the interaction volume and the final electrode is $V_R = -5654$ V. The interaction volume is a 2 mm diameter sphere. For $E_K = 5690$ eV, only a few electrons hit the inner walls of the flight-tube and when they enter the Einzel-lens region, they are focused toward the detector. For $E_K = 5660$ eV that is just 6 eV above threshold, electrons outside a narrow solid angle are deflected to the flight-tube inner walls already in, or just after, the retardation region, thus defining a limit on how low electron kinetic energies, we can detect with a certain voltage setting. Figure 2(c) presents TOF simulations of Kr 1s electrons with photon energies in the range 19 997–20 047 eV, which corresponds to kinetic energies 5670–5720 eV. In the simulation, 400 electrons are emitted in a uniform distribution 0.04 sr in the direction of the detector. Dashed black lines show simulations with discrete kinetic energies and thus, represent the instrumental broadening that is primarily dependent on the interaction volume and the detection angle of the device. Solid red lines show the simulation of kinetic energies that belong to a Voigt distribution with the natural line-broadening contribution of Kr 1s, which is $\Gamma = 2.65$ eV and the known spectral bandwidth contribution $G = 2.5$ eV from the Si(111) crystal monochromator. Figure 2(d) black solid line shows the simulated instrumental broadening FWHM in eV as a function of E_K. The black dashed line shows the reconstructed spectra FWHM in eV as a function of E_K. Clearly, the instrumental broadening becomes more severe for higher E_K. The simulation demonstrates that for lower kinetic energies, the instrumental broadening becomes less dominating with the advantage that the actual electron kinetic energy distribution is better represented by the measured spectrum. Figure 2(d) red solid line shows the detection angle that is found to be 0.019 ± 0.001 sr for kinetic energies exceeding 5670 eV, which corresponds to ~200 electrons hitting the detector. For lower kinetic energies, the acceptance angle decreases steeply so that very few electrons reach the detector.

Without any applied voltages, the relativistic kinetic energy as a function of TOF is

$$E_K = m_e c^2 \cdot \left(\frac{1}{\sqrt{1 - \frac{L^2}{T^2 \cdot c^2}}} - 1 \right), \qquad (1)$$

where c is the speed of light, m_e is the electron rest mass, L is the distance the electrons travel, and T is the TOF. For the electron

TABLE I. Photoelectron binding energy (E_B) and Lorentzian natural line broadening (Γ) in eV for the typical target gases: xenon and krypton.

Orbital	Xenon		Krypton	
	E_B (eV)	Γ (eV)	E_B (eV)	Γ (eV)
1s	34 565.13[28]	9.6[34]	14 327[36]	2.65[36]
2s	5 452.57[28]	2.76[33]	1 921.4[28]	4.28[27]
2p$_{1/2}$	5 106.72[28]	2.79[33]	1 730.90[28]	1.31[27]
2p$_{3/2}$	4 786.47[28]	2.60[33]	1 679.07[28]	1.17[27]
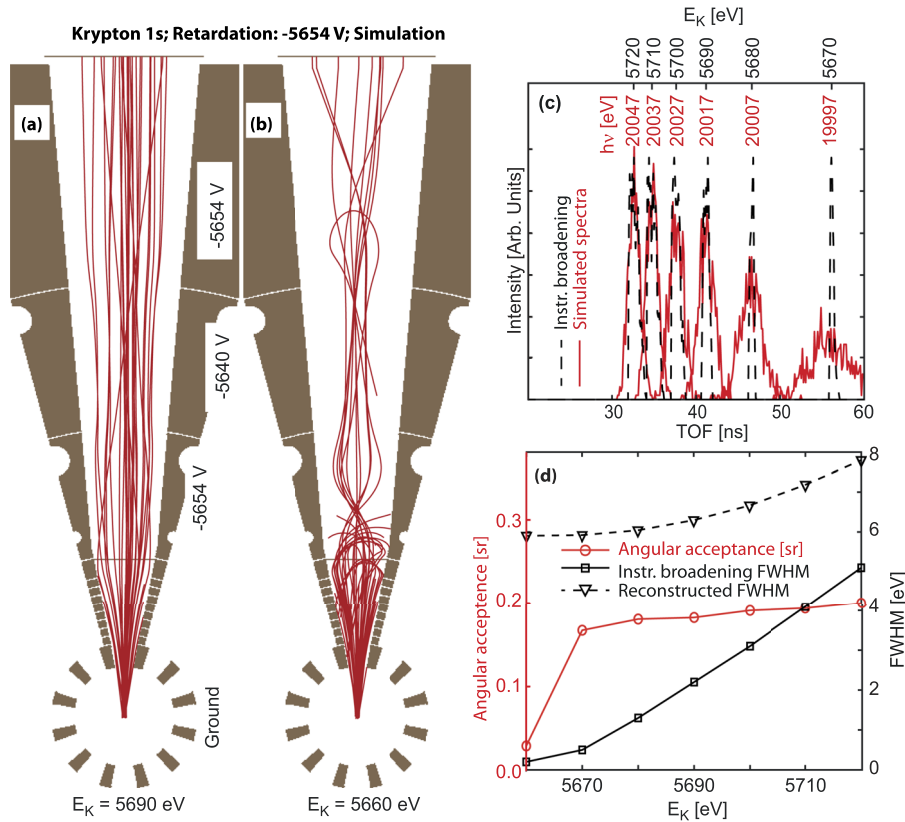
FIG. 2. (a) and (b) Cross section view of electron trajectory simulations in one flight-tube for fixed retardation voltage at E_K: 5690 and 5660 eV. Red lines are electron traces that start in the interaction region and are decelerated in the flight-tube before reaching the detector. (c) Simulated Kr 1s spectra around 20 keV photon energy with fixed retardation voltage at −5654 V. Dashed black lines present instrumental broadening. Solid red lines are complete simulated spectra. (d) Solid black line is FWHM of instrumental broadening. The dashed black line is the FWHM of the reconstructed spectrum. The solid red line is angular acceptance in steradians.

velocities that we typically work with, the first two terms of a Taylor expansion give an adequate approximation of the kinetic energy so that

$$E_K \approx \frac{m_e}{2} \cdot \frac{L^2}{T^2} + \frac{3m_e}{8c^2} \cdot \frac{L^4}{T^4}. \tag{2}$$

To provide spectral distribution, a mapping function must be constructed that converts TOF to kinetic energy for the applied retardation. Due to field penetration in the flight-tubes, instead of Eq. (2), we derive a generalized expression,

$$E_K \approx P_R + \frac{m_e}{2} \cdot \frac{P_L^2}{(T + P_T)^2} + \frac{3m_e}{8c^2} \cdot \frac{P_L^4}{(T + P_T)^4}, \tag{3}$$

where P_R is a parameter that is related to the retardation voltage, P_L is related to flight-tube length, and P_T is related to the shift in TOF. The three parameters that are characteristic for a certain retardation voltage can be found via a fitting procedure. Thus, the simulated spectra enable us to define a calibration function that transforms TOF to electron kinetic energy and further on to spectral distribution regardless of the target gas. The kinetic energy scale of the electron spectra was in addition calibrated by measuring the well-established Kr LMM Auger lines,[37] thus confirming the simulations reliability for TOF to E_K calibration.

III. RESULTS AND ANALYSIS

Figure 3 shows TOF spectra at different photon energies for the target gas xenon for a detector orientated at 0°. Photon energies were selected in small steps around 13.5 keV by tuning the undulator and monochromator together. The polarization is linear horizontal. The total xenon ionization cross-section at these photon energies is ∼0.02 Mb. Pressure in the chamber was 1.9×10^{-5} mbar. In Fig. 3(a), the flight-tube retardation was set to −8041 V. The signal from scattered light defines a prompt that represents the instant of ionization subtracted with 0.83 ns due to the time it takes photons to reach the detectors. After the prompt, four photoelectron lines are visible. Longer TOF represents lower E_K. The peak at 5 ns is due to valence electrons. The two narrow peaks between 10 and 15 ns are assigned as $2p_{1/2}$ and $2p_{3/2}$ photo lines. Above 30 ns, we have the Xe 2s line with binding energy 5452.57 eV. Xe 2s photoelectrons are, in the retardation region, decelerated from very high kinetic energies—around 8 keV—to only a few 10 eV when they enter the Einzel region where they are focused to the detector. Indeed, this dramatic retardation is required to achieve strong temporal dispersion and subsequently good spectral resolution for high kinetic energy electrons. In Fig. 3(b), we plot, in addition to the spectra at photon energies 13 530 and 13 540 eV, also their sum where the two distinguished peaks provide a means to estimate the resolving power of the spectrometer. Peaks separated with ∼10 eV are clearly shifted in TOF from which we conclude the resolving power at 8 keV kinetic energy to be $\frac{E_K}{\Delta E} \approx 800$, where E_K
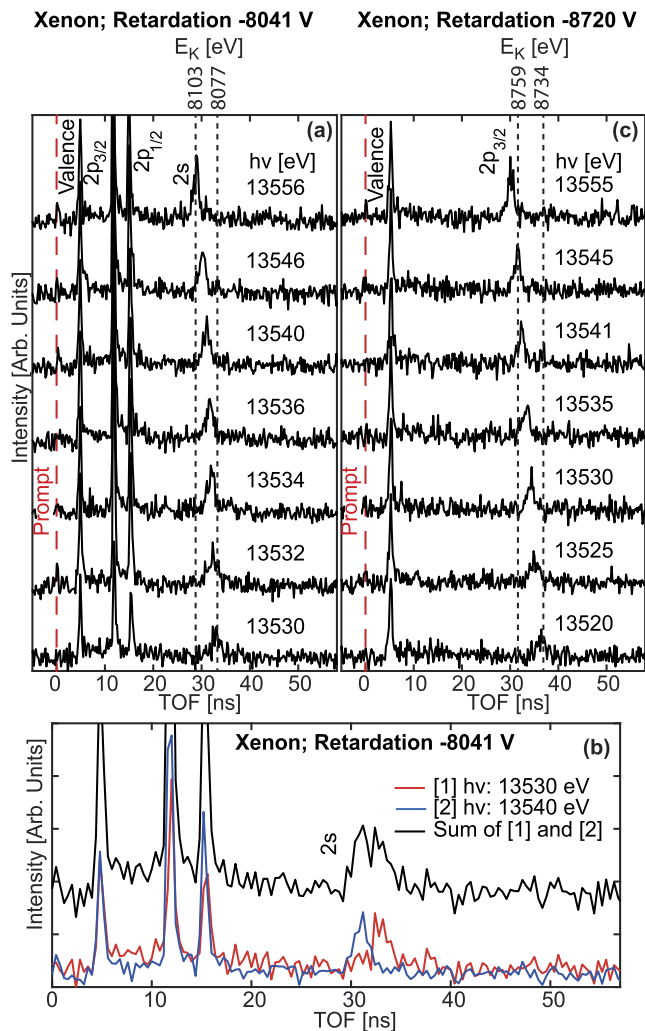
FIG. 3. Xenon TOF spectrum at several different incident photon energies around 13.5 keV for two different voltage settings. The vertical red dashed line indicates prompt. (a) $V_R = -8041$ V: Xe 2s spectra are decelerated to a low kinetic energy leading to longer TOF and subsequently better spectral resolution. In addition, $2p_{1/2}$ and $2p_{3/2}$ lines are detected. (b) We plot the spectra for photon energies 13 530 eV (red solid line) and 13 540 eV (blue solid line) above each other and their sum (black solid line). The sum of the two kinetic energies with 10 eV separation shows a two peak structure, which demonstrates the resolving power of the instrument. Binning was used for better signal to noise. (c) $V_R = -8720$ V: Only Xe $2p_{3/2}$, photoelectrons have sufficient kinetic energy to be detected and can be used for photon diagnostics.

power of ~10 eV. Indeed, all three xenon photo lines 2s, $2p_{1/2}$, and $2p_{3/2}$ are suitable for photon diagnostics. $2p_{3/2}$ has the advantage of higher cross-section and smaller natural line broadening. On the other hand, 2s has the advantage of higher binding energy, which means lower retardation voltage can be applied. Furthermore, Xe 2s has the photon energy independent anisotropy parameter, $\beta = 2$, which makes it more suitable for polarimetry. The photon energies presented in Fig. 3 are calibrated based on the procedure described in Sec. II B.

For photon energies above the Kr 1s ionization, krypton becomes the most suitable target gas. HAXPES Kr 1s photoelectron spectrum was recorded by Boudjemia *et al.* at the *SPring-8* synchrotron using 19 992 eV photon energy with bandwidth 2.29 eV, and electron energy analyzer resolution was 360 meV.[36] They extract the binding energy 14 327 eV and Lorentzian width of 2.65 eV from the spectrum. Figure 4(a) presents Kr 1s TOF spectra for photon energies close to 20 keV. At this photon energy, we have $\sigma = 0.008$ Mb. Solid black lines are experimental data, and red dashed lines are simulated spectra as described in Sec. II B. Figure 4(b) presents the data transformed to the spectral distribution. The overall line-broadening is ~6.3 eV. The resolution at 20 keV photon energy is found to be ≤10 eV, which considering that it includes the spectral bandwidth and the natural line broadening must be considered as an upper bound, see Appendix for details.
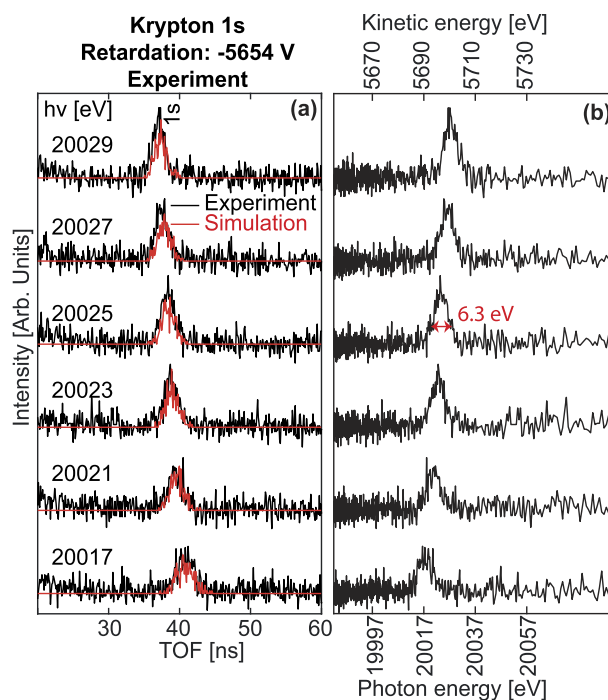
FIG. 4. Kr 1s spectra collected around 20 keV photon energy with fixed retardation voltage at −5654 V. (a) Solid black line is experimental data, solid red line is simulated data. (b) TOF data transformed to spectral distribution according to Eq. (3).

is electron kinetic energy and ΔE is the peak separation. A systematic approach for determining a metric for the resolving power is explained in Appendix. Figure 3(c) presents data in approximately the same photon energy region, but with fixed retardation voltage at −8720 V. The higher retardation voltage discriminates against electrons from the higher binding energy orbitals, and as a consequence, only $2p_{3/2}$ is detected. In addition, here we estimate a resolving

For the spectrometer to be valuable as a photon diagnostics device at EuXFEL, it is imperative that it can perform single pulse diagnostics. In the 40 bunches mode, at 100 mA, P09 beamline at PETRA III provides ~10^5 photons per pulse. SASE1 beamline at EuXFEL provides ~10^{12} photons per pulse. We estimate that at P09 we must collect data from $\frac{10^{12}}{10^5} = 10^7$ pulses in order to reach comparable statistics as at the EuXFEL. All spectra in Figs. 3 and 4 correspond to ~10^7 pulses. The integrated number of collected photoelectrons in the peak for diagnostics that is in the TOF window 28 ns–42 ns is typically ~200, which is sufficient to calculate the mean-value and standard deviation of the spectral distribution.

Figure 5(a) presents TOF spectrum for krypton at photon energies close to 15 keV with $\sigma \approx 0.018$ Mb. The retardation voltage was fixed at −608 V. The low initial kinetic energy for Kr 1s results in a resolving power of ~5 eV. The lines around 15 ns are LMM Auger lines, which have been assigned from studies with direct electron impact[37,38] and more recently studied with Synchrotron radiation and also theoretically.[36,39,40] The presence of Auger lines that are photon energy independent provides us with an intrinsic TOF to kinetic energy calibration. Furthermore, their polarization independence makes Auger lines suitable for the normalization of detector signals for polarimetry.[41,42] Figure 5(b) presents Auger spectrum at a higher retardation voltage (−1172 V) where many LMM line groups corresponding to transitions from vacancies in the L_2 and L_3 subshell can be resolved. Most dominating are $L_{2,3}M_{4,5}M_{4,5}$ but also $L_{2,3}M_{2,3}M_{4,5}$ have sufficient signal to noise ratio to be detected. Lower E_K leads to better resolution. Indeed,

for the $L_3M_{2,3}M_{4,5}$ line group, two bands can be resolved, each corresponds to transitions to several different final states, dominated by $^1F_3$ and $^3D_3$.[37] In Fig. 5(c), we have transformed the spectrum from TOF to kinetic energy with the calibration function based on simulations. Figure 5(d) shows simulated TOF to E_K calibration curves for three different voltage settings compared with measured data from Kr LMM Auger lines. The agreement is excellent, thus we use Auger lines to confirm that our calibration procedure is correct.

Although the spectrometer has 12 flight-tubes, it was during these measurements equipped with only four detectors. The presence of four detectors in different orientations with respect to the polarization vector of light enables polarization studies. Figure 6(a) shows krypton spectra at 15 keV with retardation voltage −372 V in the orientations 0°, 30° and 90°. Detector at position 180° was also used but is not presented. Auger lines are used to normalize the spectra. Kr 1s peak with the anisotropy parameter, $\beta = 2$, is most intense at 0° and is vanished at 90°. The squares in the polar plot in Fig. 6(b) represent the peak integrals over Kr 1s after background subtraction. We have fitted to the data a polarization function P, which describes the intensity as a function of the polar angle θ,[10]

$$P(\theta) = 1 + \frac{\beta}{4}\left(1 + 3 \cdot P_{Lin}\cos(2(\theta - \psi))\right). \tag{4}$$

P_{Lin} is the linear polarization component and ψ is the tilt angle. For perfect horizontal polarization, we expect $P_{Lin} = 1$ and $\psi = 0$.
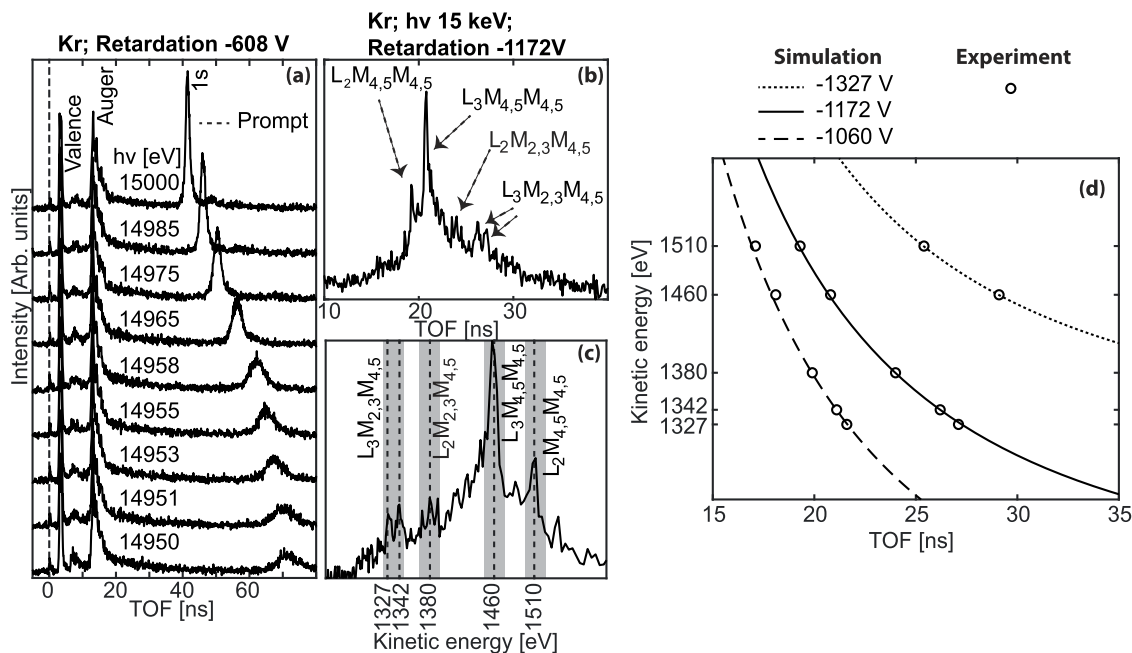
FIG. 5. (a) Spectra collected at around 15 keV photon energy with target gas krypton. Kr 1s and Auger lines are visible. (b) Resolved Kr LMM Auger lines at $h\nu$ = 15 keV and V_R = −1172 V. (c) Kr LMM Auger lines transformed to E_K scale from calibration function based on simulations. Excellent agreement is found between simulation and experimental data. (d) Comparison of simulated TOF to E_K calibration for different voltage settings and measured data from Kr LMM Auger lines.

Krypton; hv: 15 keV; Retardation: -372 V
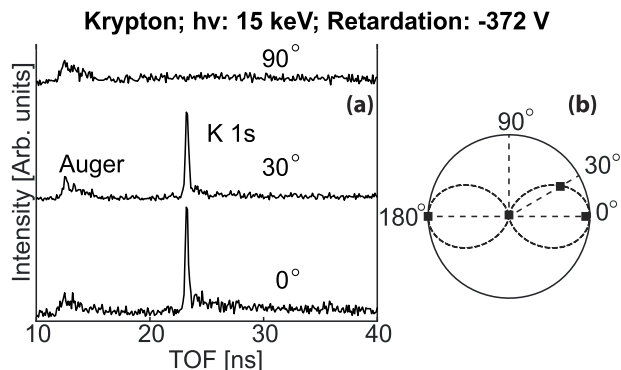
FIG. 6. (a) Kr 1s spectra were collected at 15 keV photon energy with four detectors in the orientations 0°, 30°, 90°, and 180° (180° not presented). Auger lines are used to normalize the spectra. (b) A polar plot of normalized signal intensity from the four detectors demonstrates that polarization of incoming x-rays is linear horizontal.

We measure the values $P_{Lin} = 0.97 \pm 0.03$ and $\psi = -0.00 \pm 0.03$. Note that this technique is only capable of determining the linear polarization, in contrast to invasive multilayer based polarimetry where the complete Stokes vector is found.[43]

IV. CONCLUSIONS AND OUTLOOK

We have built and tested a novel design of an angular resolved photon electron spectrometer based on the eTOF concept for the hard x-ray regime. A resolving power of ~10 eV for up to 8.7 keV electron kinetic energy has been demonstrated, and we have shown that the instrument is suitable for hard x-ray photon diagnostics for both spectral distribution and polarization. By comparing Auger lines with simulated spectra, we have confirmed that simulations are reliable for kinetic energy calibration.

AUTHOR DECLARATIONS

Conflict of Interest

The authors have no conflicts to disclose.

Author Contributions

Joakim Laksman: Conceptualization (equal); Formal analysis (equal); Methodology (equal); Visualization (equal); Writing – original draft (equal); Writing – review & editing (equal). **Florian Dietrich**: Methodology (equal). **Jia Liu**: Software (equal). **Theophilos Maltezopoulos**: Investigation (equal); Writing – review & editing (equal). **Marc Planas**: Investigation (equal); Methodology (equal). **Wolfgang Freund**: Investigation (equal). **Randeer Gautam**: Software (equal). **Naresh Kujala**: Supervision (equal). **Sonia Francoual**: Funding acquisition (equal); Supervision (equal); Writing – review & editing (equal). **Jan Grünert**: Funding acquisition (equal); Project administration (equal); Resources (equal); Supervision (equal).

DATA AVAILABILITY

The data that support the findings of this study are available from the corresponding author upon reasonable request.

APPENDIX: RESOLVING POWER

A systematic approach to determining the resolving power of the instrument is presented in Fig. 7. Spectra at photon energies 20 017 eV (red line) and 20 027 eV (blue line) are presented together with fitted Voigt functions where the Lorentzian contribution is the known natural line broadening and the Gaussian contribution is dominated by the known spectral bandwidth and the instrumental broadening. Instrumental line broadening in the recorded kinetic

Krypton 1s; Retardation: -5654 V Experiment
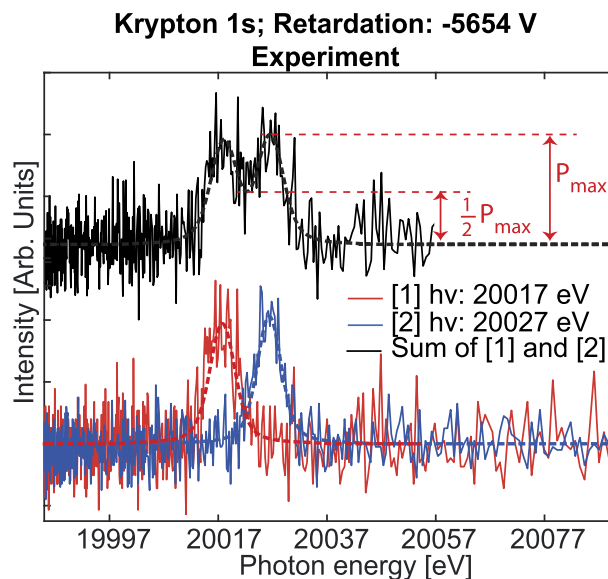
FIG. 7. Kr 1s spectra for photon energies 20 017 eV (red solid line) and 20 027 eV (blue solid line) together with fitted Voigt functions with fixed retardation voltage at −5654 V and sum of the two spectra (black solid line) with the sum of the two Voigt functions. A systematic approach to measure the resolving power of the instrument is to find the E_K separation of two spectra where the fitted two-peak Voigt function has a valley that is half the peak maximum.

energy window was from the fitting determined to be ~2.5 eV. Black solid line presents their sum to which we fit a two-peak Voigt function, with the same line broadening parameters as in the single peak spectra.

When the lowest point in the valley between the peaks is half of the peak height (P_{max}), we define the peaks as being separated. At 20 keV photon energy, we have thus demonstrated that peaks with 10 eV difference are well resolved. It must be stated that this method does not take into account the photon bandwidth or the intrinsic natural broadening and, thus, provides only a lower bound for the resolving power we can achieve.

REFERENCES

[1]P. Juranić, J. Rehanek, C. A. Arrell, C. Pradervand, R. Ischebeck, C. Erny, P. Heimgartner, I. Gorgisyan, V. Thominet, K. Tiedtke, A. Sorokin, R. Follath, M. Makita, G. Seniutinas, C. David, C. J. Milne, H. Lemke, M. Radovic, C. P. Hauri, and L. Patthey, "SwissFEL Aramis beamline photon diagnostics," J. Synchrotron Radiat. **25**, 1238–1248 (2018).

[2]J. Feldhaus, M. Krikunova, M. Meyer, T. Möller, R. Moshammer, A. Rudenko, T. Tschentscher, and J. Ullrich, "AMO science at the FLASH and european XFEL free-electron laser facilities," J. Phys. B: At., Mol. Opt. Phys. **46**, 164002 (2013).

[3]J. Ullrich, A. Rudenko, and R. Moshammer, "Free-electron lasers: New avenues in molecular physics and photochemistry," Annu. Rev. Phys. Chem. **63**, 635–660 (2012).

[4]J. Grünert, M. P. Carbonell, F. Dietrich, T. Falk, W. Freund, A. Koch, N. Kujala, J. Laksman, J. Liu, T. Maltezopoulos, K. Tiedtke, U. F. Jastrow, A. Sorokin, E. Syresin, A. Grebentsov, and O. Brovko, "X-ray photon diagnostics at the European XFEL," J. Synchrotron Radiat. **26**, 1422–1431 (2019).

[5]T. Maltezopoulos, F. Dietrich, W. Freund, U. F. Jastrow, A. Koch, J. Laksman, J. Liu, M. Planas, A. A. Sorokin, K. Tiedtke, and J. Grünert, "Operation of X-ray gas monitors at the European XFEL," J. Synchrotron Radiat. **26**, 1045–1051 (2019).

[6]A. A. Sorokin, Y. Bican, S. Bonfigt, M. Brachmanski, M. Braune, U. F. Jastrow, A. Gottwald, H. Kaser, M. Richter, and K. Tiedtke, "An X-ray gas monitor for free-electron lasers," J. Synchrotron Radiat. **26**, 1092–1100 (2019).

[7]J. Viefhaus, F. Scholz, S. Deinert, L. Glaser, M. Ilchen, J. Seltmann, P. Walter, and F. Siewert, "The variable polarization XUV beamline P04 at PETRA III: Optics, mechanics and their performance," Nucl. Instrum. Methods Phys. Res., Sect. A **710**, 151–154 (2013).

[8]J. Laksman, J. Buck, L. Glaser, M. Planas, F. Dietrich, J. Liu, T. Maltezopoulos, F. Scholz, J. Seltmann, G. Hartmann, M. Ilchen, W. Freund, N. Kujala, J. Viefhaus, and J. Grünert, "Commissioning of a photoelectron spectrometer for soft X-ray photon diagnostics at the European XFEL," J. Synchrotron Radiat. **26**, 1010–1016 (2019).

[9]N. Kujala, W. Freund, J. Liu, A. Koch, T. Falk, M. Planas, F. Dietrich, J. Laksman, T. Maltezopoulos, J. Risch, F. Dall'Antonia, and J. Grünert, "Hard x-ray single-shot spectrometer at the European x-ray free-electron laser," Rev. Sci. Instrum. **91**, 103101 (2020).

[10]E. Allaria, B. Diviacco, C. Callegari, P. Finetti, B. Mahieu, J. Viefhaus, M. Zangrando, G. De Ninno, G. Lambert, E. Ferrari, J. Buck, M. Ilchen, B. Vodungbo, N. Mahne, C. Svetina, C. Spezzani, S. Di Mitri, G. Penco, M. Trovó, W. M. Fawley, P. R. Rebernik, D. Gauthier, C. Grazioli, B. Ressel, A. Kivimäki, T. Mazza, L. Glaser, F. Scholz, J. Seltmann, P. Geßler, J. Grünert, A. De Fanis, M. Meyer, A. Knie, S. P. Moeller, L. Raimondi, F. Capotondi, E. Pedersoli, O. Plekan, M. B. Danailov, A. Demidovich, I. Nikolov, A. Abrami, J. Gautier, J. Lüning, P. Zeitoun, and L. Giannessi, "Control of the polarization of a vacuum-ultraviolet, high-gain, free-electron laser," Phys. Rev. X **4**, 041040 (2014).

[11]M. Braune, G. Brenner, S. Dziarzhytski, P. Juranić, A. Sorokin, and K. Tiedtke, "A non-invasive online photoionization spectrometer for FLASH2," J. Synchrotron Radiat. **23**, 10–20 (2016).

[12]S. Serkez, W. Decking, L. Froehlich, N. Gerasimova, J. Grünert, M. Guetg, M. Huttula, S. Karabekyan, A. Koch, V. Kocharyan, Y. Kot, E. Kukk, J. Laksman,

P. Lytaev, T. Maltezopoulos, T. Mazza, M. Meyer, E. Saldin, E. Schneidmiller, M. Scholz, S. Tomin, M. Vannoni, T. Wohlenberg, M. Yurkov, I. Zagorodnov, and G. Geloni, "Opportunities for two-color experiments in the soft x-ray regime at the European XFEL," Appl. Sci. **10**, 2728 (2020).

[13]P. Walter, A. Kamalov, A. Gatton, T. Driver, D. Bhogadi, J.-C. Castagna, X. Cheng, H. Shi, R. Obaid, J. Cryan, W. Helml, M. Ilchen, and R. N. Coffee, "Multi-resolution electron spectrometer array for future free-electron laser experiments," J. Synchrotron Radiat. **28**, 1364–1376 (2021).

[14]K. Li, J. Laksman, T. Mazza, G. Doumy, D. Koulentianos, A. Picchiotti, S. Serkez, N. Rohringer, M. Ilchen, M. Meyer, and L. Young, "Ghost-imaging-enhanced noninvasive spectral characterization of stochastic x-ray free-electron-laser pulses," Commun. Phys. **5**, 191 (2022).

[15]S. Düsterer, G. Hartmann, F. Babies, A. Beckmann, G. Brenner, J. Buck, J. Costello, L. Dammann, A. D. Fanis, P. Geßler, L. Glaser, M. Ilchen, P. Johnsson, A. K. Kazansky, T. J. Kelly, T. Mazza, M. Meyer, V. L. Nosik, I. P. Sazhina, F. Scholz, J. Seltmann, H. Sotoudi, J. Viefhaus, and N. M. Kabachnik, "Angle resolved photoelectron spectroscopy of two-color XUV–NIR ionization with polarization control," J. Phys. B: At., Mol. Opt. Phys. **49**, 165003 (2016).

[16]A. A. Lutman, J. P. MacArthur, M. Ilchen, A. O. Lindahl, J. Buck, R. N. Coffee, G. L. Dakovski, L. Dammann, Y. Ding, H. A. Dürr, L. Glaser, J. Grünert, G. Hartmann, N. Hartmann, D. Higley, K. Hirsch, Y. I. Levashov, A. Marinelli, T. Maxwell, A. Mitra, S. Moeller, T. Osipov, F. Peters, M. Planas, I. Shevchuk, W. F. Schlotter, F. Scholz, J. Seltmann, J. Viefhaus, P. Walter, Z. R. Wolf, Z. Huang, and H.-D. Nuhn, "Polarization control in an x-ray free-electron laser," Nat. Photonics **10**, 468–472 (2016).

[17]M. Ilchen, G. Hartmann, E. V. Gryzlova, A. Achner, E. Allaria, A. Beckmann, M. Braune, J. Buck, C. Callegari, R. N. Coffee, R. Cucini, M. Danailov, A. De Fanis, A. Demidovich, E. Ferrari, P. Finetti, L. Glaser, A. Knie, A. O. Lindahl, O. Plekan, N. Mahne, T. Mazza, L. Raimondi, E. Roussel, F. Scholz, J. Seltmann, I. Shevchuk, C. Svetina, P. Walter, M. Zangrando, J. Viefhaus, A. N. Grum-Grzhimailo, and M. Meyer, "Symmetry breakdown of electron emission in extreme ultraviolet photoionization of argon," Nat. Commun. **9**, 4659 (2018).

[18]V. Lollobrigida, G. Greco, D. Simeone, F. Offi, A. Verna, and G. Stefani, "Electron trajectory simulations of time-of-flight spectrometers for core level high-energy photoelectron spectroscopy at pulsed x-ray sources," J. Electron Spectrosc. Relat. Phenom. **205**, 98–105 (2015).

[19]G. Öhrwall, P. Karlsson, M. Wirde, M. Lundqvist, P. Andersson, D. Céolin, B. Wannberg, T. Kachel, H. Dürr, W. Eberhardt, and S. Svensson, "A new energy and angle resolving electron spectrometer – first results," J. Electron Spectrosc. Relat. Phenom. **183**, 125–131 (2011), electron Spectroscopy Kai Siegbahn Memorial Volume.

[20]J. Strempfer, S. Francoual, D. Reuther, D. K. Shukla, A. Skaugen, H. Schulte-Schrepping, T. Kracht, and H. Franz, "Resonant scattering and diffraction beamline P09 at PETRA III," J. Synchrotron Radiat. **20**, 541–549 (2013).

[21]L. Zheng, M. Cui, Y. Zhao, J. Zhao, and K. Chen, "Total photoionization cross-sections of Ar and Xe in the energy range," J. Electron Spectrosc. Relat. Phenom. **152**, 143–147 (2006).

[22]F. Wuilleumier, "Determination of mass-attenuation coefficients in krypton and xenon by continuous analysis between 8 and 0.8 keV," Phys. Rev. A **6**, 2067–2077 (1972).

[23]T. Koizumi, T. Hayaishi, T. Matsuo, K. Shima, H. Tawara, T. Tonuma, and A. Yagishita, "Photoionization cross section of xenon in the L edge region," J. Phys. Soc. Jpn. **58**, 13–16 (1989).

[24]K. Tiedtke, A. A. Sorokin, U. Jastrow, P. Juranić, S. Kreis, N. Gerken, M. Richter, U. Arp, Y. Feng, D. Nordlund, R. Soufli, M. Fernández-Perea, L. Juha, P. Heimann, B. Nagler, H. J. Lee, S. Mack, M. Cammarata, O. Krupin, M. Messerschmidt, M. Holmes, M. Rowen, W. Schlotter, S. Moeller, and J. J. Turner, "Absolute pulse energy measurements of soft x-rays at the linac coherent light source," Opt. Express **22**, 21214–21226 (2014).

[25]B. L. Henke, E. M. Gullikson, and J. C. Davis, "X-Ray interactions: Photoabsorption, scattering, transmission, and reflection at E = 50-30,000 eV, Z = 1-92," At. Data Nucl. Data Tables **54**, 181–342 (1993).

[26]C. T. Chantler, "Theoretical form factor, attenuation, and scattering tabulation for Z=1–92 from E=1–10 eV to E=0.4–1.0 MeV," J. Phys. Chem. Ref. Data **24**, 71–643 (1995).

[27]M. O. Krause and J. H. Oliver, "Natural widths of atomic K and L levels, $K\alpha$ X-ray lines and several KLL Auger lines," J. Phys. Chem. Ref. Data **8**, 329–338 (1979).

[28]R. D. Deslattes, E. G. Kessler, P. Indelicato, L. de Billy, E. Lindroth, and J. Anton, "X-Ray transition energies: New approach to a comprehensive evaluation," Rev. Mod. Phys. **75**, 35–99 (2003).

[29]A. Derevianko, W. R. Johnson, and K. T. Cheng, "Non-dipole effects in photoelectron angular distributions for rare gas atoms," At. Data Nucl. Data Tables **73**, 153–211 (1999).

[30]I. M. Band, Y. I. Kharitonov, and M. B. Trzhaskovskaya, "Photoionization cross sections and photoelectron angular distributions for x-ray line energies in the range 0.132–4.509 keV targets: $1 \leq Z \leq 100$," At. Data Nucl. Data Tables **23**, 443–505 (1979).

[31]D. Céolin, J. M. Ablett, D. Prieur, T. Moreno, J.-P. Rueff, T. Marchenko, L. Journel, R. Guillemin, B. Pilette, T. Marin, and M. Simon, "Hard x-ray photoelectron spectroscopy on the galaxies beamline at the SOLEIL synchrotron," J. Electron Spectrosc. Relat. Phenom. **190**, 188–192 (2013), recent advances in Hard X-ray Photoelectron Spectroscopy (HAXPES).

[32]M. N. Piancastelli, T. Marchenko, R. Guillemin, L. Journel, O. Travnikova, I. Ismail, and M. Simon, "Hard x-ray spectroscopy and dynamics of isolated atoms and molecules: A review," Rep. Prog. Phys. **83**, 016401 (2019).

[33]M. Oura, T. Gejo, K. Nagaya, Y. Kohmura, K. Tamasaku, L. Journel, M. N. Piancastelli, and M. Simon, "Hard x-ray photoelectron spectroscopy on heavy atoms and heavy-element containing molecules using synchrotron radiation up to 35 keV at SPring-8 undulator beamlines," New J. Phys. **21**, 043015 (2019).

[34]M. N. Piancastelli, K. Jänkälä, L. Journel, T. Gejo, Y. Kohmura, M. Huttula, M. Simon, and M. Oura, "X-ray versus Auger emission following Xe $1s$ photoionization," Phys. Rev. A **95**, 061402 (2017).

[35]S. J. Schaphorst, A. F. Kodre, J. Ruscheinski, B. Crasemann, T. Åberg, J. Tulkki, M. H. Chen, Y. Azuma, and G. S. Brown, "Multielectron inner-shell photoexcitation in absorption spectra of Kr: Theory and experiment," Phys. Rev. A **47**, 1953–1966 (1993).

[36]N. Boudjemia, K. Jänkälä, R. Püttner, T. Gejo, L. Journel, Y. Kohmura, M. Huttula, M. N. Piancastelli, M. Simon, and M. Oura, "Deep-core photoionization of krypton atoms below and above the $1s$ ionization threshold," Phys. Rev. A **101**, 053405 (2020).

[37]J. C. Levin, S. L. Sorensen, B. Crasemann, M. H. Chen, and G. S. Brown, "Krypton L-MM Auger spectra: New measurements and analysis," Phys. Rev. A **33**, 968–976 (1986).

[38]L. O. Werme, T. Bergmark, and K. Siegbahn, "The high resolution $L_{2,3}$ MM and $M_{4,5}$ NN Auger spectra from krypton and $M_{4,5}$ NN and $N_{4,5}$ OO Auger spectra from xenon," Phys. Scr. **6**, 141–150 (1972).

[39]Y. Morishita, Y. Tamenori, K. Okada, T. Oyama, K. Yamamoto, K. Tabayashi, T. Ibuki, K. Moribayashi, and I. H. Suzuki, "Formation mechanisms of multicharged kr ions through 2p shell photoionization using a coincidence technique," J. Phys. B: At., Mol. Opt. Phys. **39**, 1323–1335 (2006).

[40]N. Boudjemia, K. Jänkälä, T. Gejo, Y. Kohmura, M. Huttula, M. N. Piancastelli, M. Simon, M. Oura, and R. Püttner, "Experimental and theoretical study of the kr l-shell Auger decay," Phys. Rev. A **104**, 012804 (2021).

[41]J. Karvonen, A. Kivimäki, H. Aksela, S. Aksela, R. Camilloni, L. Avaldi, M. Coreno, M. de Simone, and K. C. Prince, "Angular distribution in xenon $M_{4,5}N_{4,5}N_{4,5}$ Auger decay," Phys. Rev. A **59**, 315–319 (1999).

[42]R. Sankari, A. Kivimäki, M. Huttula, H. Aksela, S. Aksela, M. Coreno, G. Turri, R. Camilloni, M. de Simone, and K. C. Prince, "Angular distribution in resonant Auger spectra of xenon excited below the $3d_{5/2}$ ionization threshold," Phys. Rev. A **63**, 032715 (2001).

[43]W. Grizolli, J. Laksman, F. Hennies, B. N. Jensen, R. Nyholm, and R. Sankari, "Multilayer based soft-x-ray polarimeter at MAX IV Laboratory," Rev. Sci. Instrum. **87**, 025102 (2016).